Research Article Vol. 2, No. 5 / 25 October 2024 / Optica Quantum 371

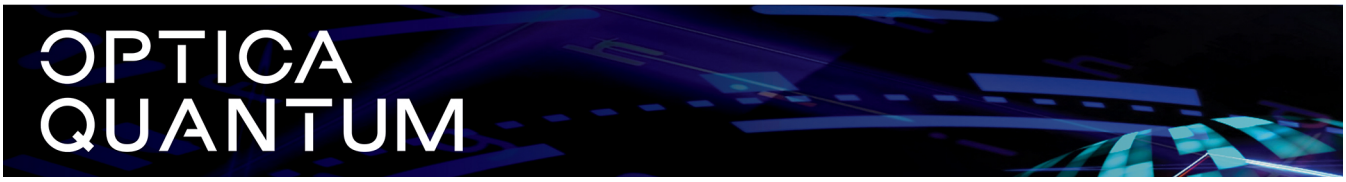

Multiqubit quantum state preparation enabled by topology optimization

A. Miguel-Torcal,[1,2] A. González-Tudela,[3] F. J. García-Vidal,[1,2,4] and A. I. Fernández-Domínguez[1,2,*]

[1]Departamento de Física Teórica de la Materia Condensada, Universidad Autónoma de Madrid, E-28049 Madrid, Spain
[2]Condensed Matter Physics Center (IFIMAC), Universidad Autónoma de Madrid, E-28049 Madrid, Spain
[3]Institute of Fundamental Physics IFF-CSIC, Calle Serrano 113b, E-28006 Madrid, Spain
[4]Institute of High Performance Computing, Agency for Science, Technology, and Research (A*STAR), Connexis, 138632, Singapore
*a.fernandez-dominguez@uam.es

Received 24 May 2024; revised 30 August 2024; accepted 25 September 2024; published 22 October 2024

Using topology optimization, we inverse-design nanophotonic cavities enabling the preparation of pure states of pairs and triples of quantum emitters. Our devices involve moderate values of the dielectric constant, operate under continuous laser driving, and yield fidelities to the target (Bell and W) states approaching unity for distant qubits (several natural wavelengths apart). In the fidelity optimization procedure, our algorithm generates entanglement by maximizing the dissipative coupling between the emitters, which allows the formation of multipartite pure steady states in the driven-dissipative dynamics of the system. Our findings open the way toward the efficient and fast preparation of multiqubit quantum states with engineered features, with potential applications for nonclassical light generation, and quantum sensing and metrology.

https://doi.org/10.1364/OPTICAQ.530865

1. INTRODUCTION

The preparation and manipulation of highly entangled multiqubit states is at the core of all quantum technologies. This makes the degree of control over qubit–qubit interactions a key aspect in the assessment of material systems for their implementation. In this context, nanophotonic devices offer a wide range of strategies to tailor photon propagation and the photonic density of states at different length scales [1,2]. This makes them stand out among other candidates for quantum hardware in terms of scalability, integration, and speed of operation [3,4]. For this reason, in recent years, photonic architectures structured at the nanoscale to harness photon-assisted interactions among quantum emitters (QEs, acting as qubits) have been proposed as the platform for applications such as quantum light sources [5–7] and detectors [8], quantum networks [9,10] and circuits [11,12], memories [13], sensors [14], or simulators [15,16].

Lately, inverse design techniques have revealed unexpected and counter-intuitive optimization pathways for nanophotonic systems [17,18]. These numerical tools have proven to be particularly successful in functionalities that require a complex trade-off between conflicting mechanisms [19–21], and their impact on the field has even opened the way toward the exploration of the fundamental limits of photonic performance [22,23] and discovery [24]. More recently, these numerical tools have also been exploited in the realm of quantum nano-optics, where a delicate balance between the engineering of light–matter near-field coupling and the shaping of radiation and absorption is required. Thus, inverse-designed quantum nanophotonic devices have shown a notable performance in the context of qubit entanglement formation [25,26] and single-photon generation [27,28].

Here, we employ topology optimization (TO) [29,30] to inverse-design dielectric cavities that enable the preparation of Bell states [31] of QE pairs. They are obtained by using the fidelity of the density matrix of the system to these target states as the optimization function, in conditions of continuous coherent pumping and inter-emitter distances of a few natural wavelengths (comparable to the cavity dimensions). By setting the laser fields driving the emitters in phase (anti-phase), antisymmetric (symmetric) Bell-like states are obtained. Our analysis of the driven-dissipative dynamics of the QEs reveals that the small differences between the state implemented in the TO cavities and the target one translates into a slight reduction in its preparation time [32]. Finally, we prove the versatility of our design strategy extending our investigation to QE triples and presenting a dielectric device that generates highly entangled tripartite states with fidelities to the symmetric W state [33] comparable with those obtained from the ad hoc optimization of the master equation parameters. Our results prove that, through a (fully classical) laser driving, inverse-designed nanophotonic devices can be used to produce purely quantum states of QE ensembles, showcasing them as a promising resource for quantum technology.

2. THEORETICAL MODEL

Our nanophotonic cavities are designed to host pairs and triples of distant QEs, modeled as two-level systems (with perfect quantum yield) under laser driving. The dynamics of the density matrix for the system, ρ, is described by a master equation of the form [34]

$$\mathcal{L}\rho \equiv \imath\Big[\rho, H\Big] + \sum_{i,j}\gamma_{ij}\left(\sigma_j\rho\sigma_i^\dagger - \frac{1}{2}\left\{\sigma_i^\dagger\sigma_j, \rho\right\}\right) = \frac{d\rho}{dt}, \quad \textbf{(1)}$$

under the assumption that the QEs are weakly coupled to their electromagnetic (EM) environment, an approximation that will be revisited below. In Eq. (1), σ_i ($\sigma_i^\dagger$) is the annihilation (creation) operator for the QE labeled as i (ranging from 1 to 2–3), fulfilling $\{\sigma_i^\dagger, \sigma_j\} = \delta_{ij}$. The Hamiltonian above can be written in the laser frame as

$$H = \sum_i \delta_i\sigma_i^\dagger\sigma_i + \sum_{i\neq j} g_{ij}\sigma_i^\dagger\sigma_j + \sum_i \Omega_i(\sigma_i + \sigma_i^\dagger), \quad \textbf{(2)}$$

where $\delta_i = \omega_i - \omega_\mathrm{L}$ is the detuning of the frequency of the emitters, ω_i, with respect to the laser frequency, ω_L. The second term in Eq. (2) reflects the coherent interaction between the QEs assisted by off-resonant EM modes with strength given by g_{ij}, and the last one, their laser driving with amplitudes Ω_i. Finally, and back to Eq. (1), the dissipative interaction between the QEs ($i \neq j$), as well as their radiative decay ($i = j$) is also accounted for by Lindblad operators weighted by the dissipative matrix (with entries γ_{ij}), which must be positive semi-definite to ensure the physical character of the system dynamics [35].

Düng *et al.* [34] established the connection between the coherent and dissipative coupling parameters in Eqs. (1), (2) and the EM dyadic Green's function [36] of the dielectric environment of the QEs, obtaining $g_{ij} = \omega^2\mathbf{p}^*\Re\{\mathbf{G}(\mathbf{r}_i, \mathbf{r}_j, \omega)\}\mathbf{p}/\hbar\varepsilon_0c^2$ and $\gamma_{ij} = 2\omega^2\mathbf{p}^*\Im\{\mathbf{G}(\mathbf{r}_i, \mathbf{r}_j, \omega)\}\mathbf{p}/\hbar\varepsilon_0c^2$, where $\mathbf{p}$ is the transition dipole moment of the QEs and $\mathbf{r}_{i,j}$ their position. This framework links the quantum dynamics of ensembles of identical emitters and the spatial distribution of the dielectric permittivity in their vicinity, $\epsilon(\mathbf{r})$, which has allowed the investigation of QE entanglement generation in different nanophotonic structures [26,37,38]. In these works, the dyadic Green's function is evaluated at the QE frequency. We employ it here to describe emitters with slightly different natural frequencies and detuned from the driving laser. We anticipate that the validity of this approach for the nanophotonic cavities that we obtain from the TO algorithm will be demonstrated below. In what follows, we will employ the laser frequency, $\omega_\mathrm{L} \simeq 2.067\,\mathrm{eV}$ ($\lambda = 600\,\mathrm{nm}$) for the evaluation of the g_{ij} and γ_{ij} parameters in our calculations.

The density matrix obtained from the solution of Eq. (1) allows for the calculation of expectation values of any physical observable of the system. In our case, we will focus on its fidelity [39], $F_\phi = \langle\phi|\rho|\phi\rangle$, to a desired pure state, $|\phi\rangle$. This quantity ranges from 0 to 1, and we will use it as a measure of the similarity of the quantum state of the QE pair/triple in our nanophotonic system to the target one. Exploiting the dependence of the master equation parameters on the permittivity of the medium hosting the QE through the dyadic Green's function, we have developed an inverse design algorithm based on TO that provides the optimum (lossless, real-valued) dielectric map, $\epsilon(\mathbf{r})$, for a given target state $|\phi\rangle$ by maximizing F_ϕ. A detailed description of the numerical method can be found elsewhere [26], we only sketch it here. Inspired by recent reports [40–42], it consists of a nested iterative procedure in which $\epsilon(\mathbf{r})$ is shaped with the precision of the spatial discretization used to solve Maxwell's equations. Starting from free space, in each iteration, the effect of a small, local increment of the permittivity, $\delta\epsilon$, on the target function is assessed for each mesh element. By keeping only those that contribute to enlarge F_ϕ, dielectric cavities with optimum performance (for a set of given constraints) are attained. The high speed and efficiency of the algorithm resides in the use of first-order Born scattering series and the exploitation of Lorentz reciprocity in the evaluation of the effect of the local dielectric variations on the dyadic Green's functions [36].

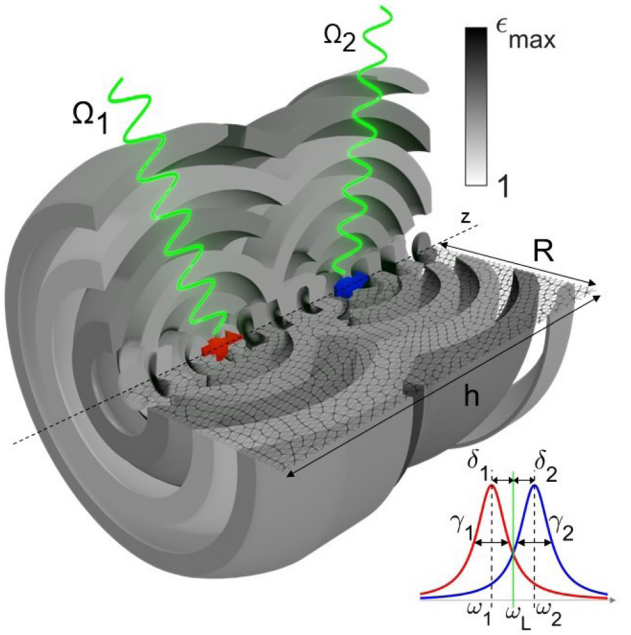

Fig. 1. TO-designed nanophotonic cavity, of radius R and height h, hosting a QE pair. The emitters are aligned and oriented along the z-direction, and driven coherently by laser fields of amplitude Ω_i (wavy green lines). The light gray mesh renders the spatial discretization in the solution of Maxwell's equations, and the permittivity map is coded from white (vacuum) to black ($\epsilon = \epsilon_\mathrm{max}$). The bottom-right illustrates the spectral position and Lorentzian-type line shapes of the QEs, with their linewidths and detunings with respect to the laser frequency ω_L.

Figure 1 illustrates an inverse-designed cavity hosting a QE pair. The TO algorithm is interfaced with the finite-element EM solver implemented in Comsol Multiphysics™, whose spatial discretization is sketched by the dark gray thin mesh. The QEs are separated a distance d_{12} along the z-direction, with their dipole moments parallel to it. This emitter configuration allows us to exploit the azimuthal symmetry of the system to solve Maxwell's equations within the rz-plane only. As a result, we obtain cylindrical cavities with rotational symmetry, radius R, and height h. The dielectric function varies from 1 (white) to its maximum, ϵ_max (black), which varies from one design to another. We set a threshold, $\epsilon_\mathrm{max} \leq 9$, corresponding to semiconductor materials such as GaP [43] in the visible range, to remain in the typical parameter regime of nanophotonics. In the bottom right corner, the line shape of the two emitters is represented, with natural frequencies ω_i and linewidths $\gamma_i = \gamma_{ii}$. Both are detuned from the laser frequency ω_L.

3. RESULTS

First, we design dielectric cavities to prepare distant QE pairs into maximally entangled pure states in the steady-state regime, $\mathcal{L}\rho = 0$ in Eq. (1). We set the dimensions of the structures to $R = 6.25\lambda$ and $h = 16.67\lambda$ ($\lambda = 600$ nm), and the dipole moment of the emitters to $|\mathbf{p}| = 1\, e{\cdot}$nm, which yields a free-space decay rate $\gamma_0 = \omega^3|\mathbf{p}|^2/3\pi\hbar\epsilon_0 c^3 = 2.3\,\mu$eV. We choose the even and odd Bell states,

$$|+\pm\rangle = \frac{1}{\sqrt{2}}\big[|ge\rangle \pm |eg\rangle\big], \tag{3}$$

as our target, with g (e) indicating the ground (excited) state of each QE, and generate two different sets of devices, resulting from the maximization of the corresponding fidelities, $F_{+\pm}$. In accordance with recent literature [44], we make the detunings of the QE frequencies symmetric with respect to the laser frequency, and significantly smaller than their linewidth, $|\delta_i|/\gamma_0 = 0.2$ ($i = 1, 2$). The laser pumping strengths are set to $|\Omega_i|/\gamma_0 = 0.7$, and their parity is given by the symmetry of the target state, having $\Omega_1 = \mp\Omega_2$ for $|+\pm\rangle$. The diffraction limit of classical optics imposes a lower bound for the inter-emitter distance, $d_{12} \gtrsim \lambda/2$, to make a reliable control over the two laser fields possible.

Figure 2 analyzes the performance of the inverse-designed cavities obtained for inter-emitter distances between λ and 4λ,

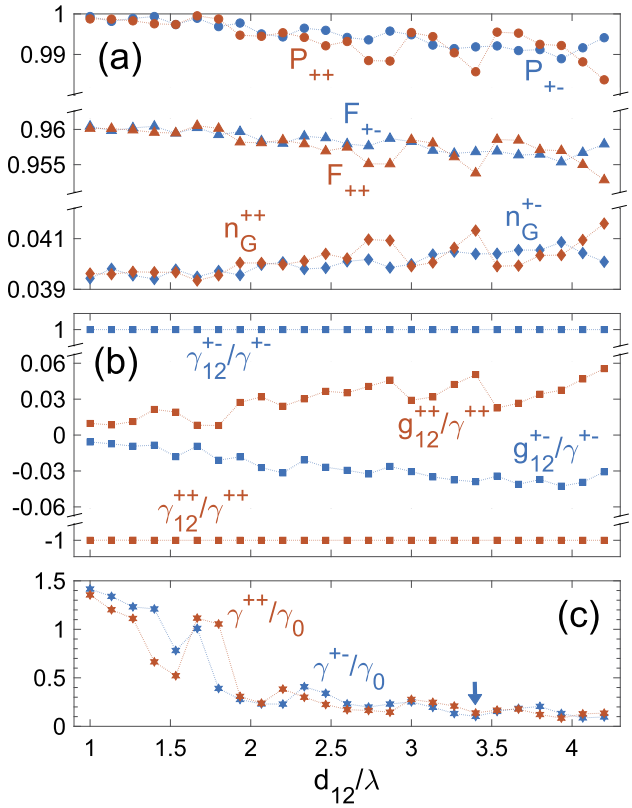

Fig. 2. (a) Fidelity to even and odd Bell states, $F_{+\pm}$, versus inter-emitter distance for TO cavities with $R = 6.25\lambda$ and $h = 16.67\lambda$. Purity, $F_{+\pm}$, and ground state population, $n_G^{+\pm}$, of the attained states. The detuning and pumping parameters are $|\delta_i|/\gamma_0 = 0.2$ and $|\Omega_i|/\gamma_0 = 0.7$. (b) Dissipative, γ_{12}, and coherent, g_{12}, coupling strengths normalized to the QEs decay rate, $\gamma = \sqrt{\gamma_1\gamma_2}$, as a function of d_{12} for same devices as panel (a). (c) Purcell factor, γ/γ_0, versus emitter–emitter distance for all the cases above. The blue arrow indicates the configuration considered in Figs. 3 and 4.

and targeting even (in orange dots) and odd (in blue dots) Bell states. In Fig. 2(a), the fidelities (used as optimization functions) are shown in connected triangles. We obtain $F_{+\pm}>0.95$ for all emitter–emitter distances and both symmetries. The small deviation from unity is caused by the finite size of the devices, which we restrict to the micron scale to remain in the domain of nanophotonics technology. This is manifested in the slight decreasing trend of the fidelity as a function of d_{12} for both sets of data, and the fact that, in some cases, the TO algorithm was terminated because the maximum permittivity condition, $\epsilon_{\max} = 9$, was reached in some position within the device. Importantly, all our cavities include a cylindrical $\epsilon = 1$ void around each of the QEs (of height 5 nm and radius 2.5 nm) that the TO algorithm does not explore, which makes their performance robust against emitter misplacement within a few-nanometer range.

To clarify the nature of the quantum states sustained by the TO cavities, their purity is plotted in connected circles in Fig. 2(a). This is calculated as $P_{+\pm} = \mathrm{Tr}\{\rho_{+\pm}^2\}$, where $\rho_{+\pm}$ is the system density matrix (the subscripts indicate the target Bell state). We can observe that it is above 0.98 in all cases, indicating the pure character of the states formed in the devices [45]. Note as well that the purities present a decreasing slope very similar to $F_{+\pm}$. The deviation of $\rho_{+\pm}$ from the Bell states in Eq. (3) becomes clearer by computing the ground state populations, $n_G^{+\pm} = \langle gg|\rho_{+\pm}|gg\rangle$. They are rendered in rhombuses in Fig. 2(a), obtaining $n_G^{+\pm} \sim 0.04$ and a positive slope with increasing distance. Again, this indicates that the radiation losses experienced by the TO cavities due to their micron-sized dimensions are behind the failure to obtain $|+\pm\rangle$ with higher accuracy.

Once we have verified the capability of the cavities to produce highly entangled steady states for QEs several laser wavelengths apart, we explore the physical mechanism behind their operation. For this purpose, we plot in Fig. 2(b) the coherent and dissipative coupling strengths versus d_{12}. Both are normalized to the collective decay rate of the system, defined as $\gamma = \sqrt{\gamma_1\gamma_2}$ [46]. We can observe that the dissipative coupling is maximized [47], reaching absolute values equal to this collective decay, $|\gamma_{12}^{+\pm}|/\gamma^{+\pm} = 1$, and its sign is positive (negative) for odd (even) target Bell states. Note that we are using the $++$ and $+-$ superscripts to indicate that the parameters correspond to cavities implementing even and odd Bell states, respectively. However, $g_{12}^{+\pm}$ acquires vanishing values, with opposite sign to $\gamma_{12}^{+\pm}$. These values tend to reproduce the master equation parameters previously reported in theoretical proposals for emitter entanglement through cavity or waveguide dissipation [44,48–54]. In all these proposals, however, the free-space emission was only considered phenomenologically as an extra parameter, but no realistic calculation was performed. In the proposal with plasmonic waveguides [38], such a factor was taken into account showing how their ability to suppress far-field emission offers a feasible realization for this dissipative entanglement mechanism. However, this came at the expense of high absorption losses, which effectively restricts the QE–QE distances to the sub-wavelength regime. To our knowledge, our TO dielectric cavities are the first platforms that implement efficiently this phenomenon for distant emitters thanks to the ability to optimize both the generation of long-range interactions and the suppression of the far-field emission at the same time.

Our TO algorithm is able to produce dielectric cavities that operate efficiently within a wide range of inter-emitter distances. To keep the ratio $\gamma_{12}^{+\pm}/\gamma^{+\pm}$ at its maximum value for all d_{12}, they must modulate the QE radiation into free-space in different ways. This is shown in Fig. 2(c), which plots the Purcell factor, $\gamma^{+\pm}/\gamma_0$,

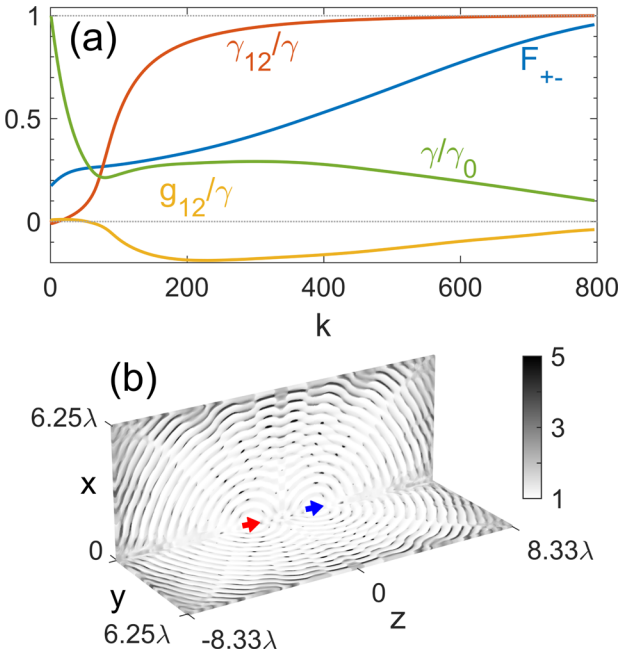

Fig. 3. (a) Fidelity, normalized coupling strengths, and Purcell factor versus iteration step for the TO cavity targeting the odd Bell state for $d_{12} = 3.4\lambda$. (b) Permittivity map obtained as a result of the TO procedure in panel (a). The dielectric constant is represented in gray scale between 1 (white) and 5 (black). The red and blue arrows indicate the position and orientation of the QEs.

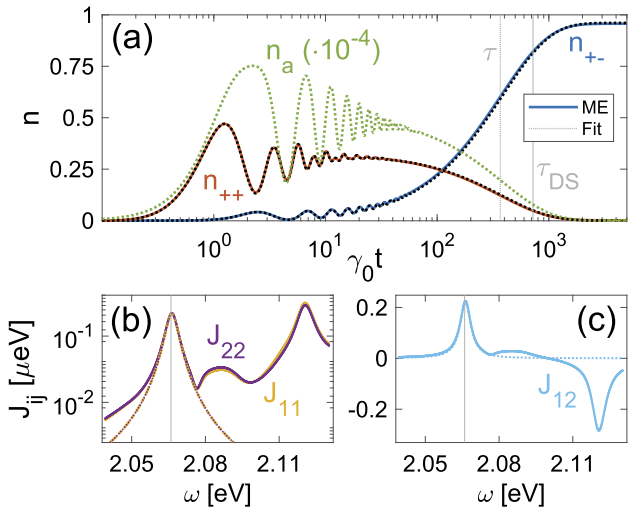

Fig. 4. (a) Population dynamics of the QE pair within the TO cavity in Fig. 3(b) under even coherent driving and initially in their ground state, $n_G(0) = 1$. The transients obtained from Eqs. (1) and (5) are rendered in color solid and black dotted lines, respectively. Vertical gray lines indicate the preparation times of the TO steady state, τ, and the phenomenological pure dark state, τ_{DS}. Panels (b) and (c) show the spectral density at the emitters position (yellow, purple) and the cross-spectral density (light blue). Dotted lines render their single-mode fitting at the laser frequency (vertical line).

for all the cavities in the panels above. At small distances, the dissipative coupling is strong and the emission rate of the QEs is Purcell-enhanced (by a factor 1.5) to achieve a maximal fidelity. In contrast, for large d_{12}, the QE interactions are weak, requiring a strong reduction in their decay rate and yielding $\gamma^{+\pm}/\gamma_0 \simeq 0.1$. As anticipated, the devices showcase a 15-fold difference in the Purcell factor, which is key for the formation of dissipatively entangled quantum states with similar $F_{+\pm}$ for QEs separated by very different distances.

Having assessed the performance of the TO cavities for Bell state preparation, we focus next on different aspects of the inverse-design procedure. To do so, we select a particular device, indicated by the blue vertical arrow in Fig. 2(c) ($d_{12} = 3.4\lambda$, odd symmetry), and use it as a test bed for the inspection of the operation of our optimization algorithm. Figure 3(a) plots the fidelity to the target state (blue line), the coupling strengths (red and yellow lines), and the collective Purcell factor (green) versus the iteration step k. Each step corresponds to a complete scan within the rz-section of the cavity, evaluating the Green's function and consolidating or discarding a $\delta\epsilon = 0.003$ increment in each mesh point. Three different regimes can be distinguished in the evolution of these quantities along the iterative procedure toward the condition $F_{+-} = 1$. First, a sharp drop in the Purcell factor takes place, while both couplings grow slowly in absolute value and different sign. Between the steps 100 and 300, γ/γ_0 varies very little, while γ_{12}/γ increases quickly, approaching its maximum, and g_{12} reaches its minimum value. For k>300, both the Purcell factor and coherent coupling tend smoothly to 0, while the dissipative coupling, already very close to the condition $\gamma_{12}/\gamma = 1$, converges toward it. In all this process, the fidelity grows almost linearly from 0.2 at $k = 0$ to $F_{+-} = 0.96$ at $k = 800$, when the cavity implements master equation parameters very similar to those previously reported for the formation of dissipatively entangled, dark states: $\gamma_{12} = \gamma$, $g_{12} = 0$.

The dielectric map, $\epsilon(\mathbf{r})$, of the nanophotonic cavity obtained at the end of the optimization procedure described above is shown in Fig. 3(b). The permittivity is fully characterized within the rz-plane, but to facilitate its visibility, it is displayed within xz- and yz-planes. The QEs are sketched as blue and red arrows along the z-axis. The gray scale codes the dielectric constant linearly from 1 (white) to $\epsilon_{max} = 5$ (black). Two different regions can be distinguished in $\epsilon(\mathbf{r})$. Few wavelengths apart from the QEs and near the edges of the cavity, elliptical-shaped, high-contrast periodic reflectors are apparent over a smooth $\epsilon \simeq 3$ background. These we can link to the reduction of the collective Purcell factor that minimizes the radiation decay experienced by the emitters. In their near-field and centered around them, two sets of lower-contrast, spherical-shaped shells can be observed. These are embedded into an $\epsilon \simeq 1$ background. These contribute to the tailoring of the emitter–emitter interactions, maximizing (vanishing) its dissipative (coherent) coupling. Small, deeply subwavelength, and isolated rings of high permittivity are distributed along the radial direction in between these two regions. Our TO algorithm conforms these two structural elements (far-field reflectors, and near-field shells and rings) to optimize the balance between the two mechanisms, photon-assisted interactions and photon leakage, that govern the quantum state of the QE dimer. Note that the maximum permittivity in the device acquires only a moderate value, well below the threshold set for the TO algorithm.

Figure 4(a) explores the preparation time (from the onset of the laser driving) required for the emergence of the steady state in the cavity in Fig. 3(b). It plots the population dynamics in the first excitation manifold and in the Bell state basis, $n_{+\pm}(t) = \langle +\pm|\rho(t)|+\pm\rangle$. The system is initially in its ground state, $n_G(0) = 1$. We can clearly observe that once the QE pair is pumped, the

population is transferred first into the even Bell state, and $n_{++}(t)$ (orange) develops a plateau (preceded by significant oscillations) that showcases a meta-stable regime [32] that extends up to $t \simeq 40\gamma_0^{-1}$. In this time window, $n_{+-}(t)$ is negligible. At longer times, the population of the odd Bell states grows quickly, reaching $n_{+-} \simeq 0.96$ at $t \gtrsim 10^3\gamma_0^{-1}$, which sets the preparation time for the cavity steady state. To obtain another estimation of this time, we compute the inverse of the Liouvillian gap of Eq. (1) [55,56]. The value obtained, $\tau = 350\gamma_0^{-1}$, is indicated by the vertical gray dotted line in Fig. 4(a). We can benchmark this estimation against the inverse of the Liouvillian gap for the phenomenological master equation that yields pure dark Bell states in Ref. [32], $\tau_{DS} = 700\gamma_0^{-1}$ (see vertical gray solid line). Thus, we can conclude that the small deviation from the target state in the TO cavities allows for a shorter preparation time than the exact Bell state generated under an ad hoc theoretical model.

To gain insight into the population dynamics in Fig. 4(a), we investigate next the role of the cavity fields as intermediaries of the QE–QE interactions behind them. To do so, we must refine our model of the system to account for the photonic degrees of freedom in its quantum density matrix, ϱ. Thus, we perform EM calculations for the spectral densities, $J_{ij}(\omega) = \gamma_{ij}(\omega)/2\pi$ [57] for each emitter and between them, shown in Figs. 4(b) and 4(c), respectively. In these panels, the solid lines render the EM simulations for our TO device, and dotted lines their single Lorentzian fittings [58]

$$J_{ij}(\omega) = \frac{\mathcal{G}_i\mathcal{G}_j}{\pi}\frac{\Gamma_a/2}{(\omega-\omega_a)^2+(\Gamma_a/2)^2} \tag{4}$$

in the vicinity of the laser frequency (indicated by vertical gray lines). The fitting parameters, $\mathcal{G}_1 \simeq \mathcal{G}_2 = 7.75\gamma_0 = 17.1\ \mu$eV and $\Gamma_a = 2459\gamma_0 = 5.4$ meV, yield very good agreement with the full spectra within a 0.03-eV window around ω_L (much larger than the QE detunings).

Equation (4) allows for the direct parameterization of a master equation of the form [57]

$$\begin{aligned}\mathcal{L}'\varrho \equiv \imath\left[\rho, H'\right] + \Gamma_a\left(a\varrho a^\dagger - \frac{1}{2}\left\{a^\dagger a, \varrho\right\}\right)\\ + \sum_i \gamma_0\left(\sigma_i\varrho\sigma_i^\dagger - \frac{1}{2}\left\{\sigma_i^\dagger\sigma_i, \varrho\right\}\right) = \frac{d\varrho}{dt},\end{aligned} \tag{5}$$

with $H' = (\omega_a - \omega_L)a^\dagger a + \sum_i \delta_i\sigma_i^\dagger\sigma_i + \mathcal{G}_i\sigma_i^\dagger a + \Omega_i\sigma_i^\dagger + h.c.$ It describes the coupling of both emitters to their EM environment, with strengths $\mathcal{G}_i$, approximated by a single cavity mode with frequency ω_a and linewidth Γ_a [59]. Black dotted lines in Fig. 4(a) plot the QE populations obtained with this refined model. The excellent agreement with the transients in solid lines prove the accuracy of the original description in the weak-coupling, quasi-degenerate regime ($|\delta_i| = 0.2\gamma_0 \simeq 2\gamma$) in which the inverse-designed cavity operates [60]. Moreover, the solution to Eq. (5) enables us to compute the population transient for the cavity mode, $n_a(t) = \mathrm{tr}\{a^\dagger a\varrho(t)\}$. This is rendered by the green dotted line in Fig. 4(a), and shows that the plateau in $n_{++}(t)$ coincides with the time window in which the cavity population is non-negligible. Thus, the cavity mode sustains this meta-stable regime in the quantum dynamics, beyond which, its population decays and the two QEs, already in the target Bell state, become effectively decoupled from their EM environment.

Up to here, we have designed nanophotonic cavities to host quantum states of QE pairs, but our TO algorithm can be applied to any emitter ensemble. As discussed above, the limiting factor is the calculation of the EM dyadic Green's function, which is greatly simplified if the QEs are aligned. Thus, to prove the versatility of our method, we consider now QE triples, located along the z-axis and with dipole moments parallel to it. There exist multiple ways to generate entanglement in tripartite systems, which have been the object of much research in recent years [61,62]. We focus on a well-known class of three-qubit states, the so-called W states [63,64]. These are a class of pure states that present high robustness against noise and losses, which means that they retain the maximum possible amount of bipartite entanglement when any one of the three QEs is lost (traced out) [33]. In particular, we take the symmetric W state

$$|{+}{+}{+}\rangle = \frac{1}{\sqrt{3}}\left[|gge\rangle + |geg\rangle + |egg\rangle\right], \tag{6}$$

as the target for our TO algorithm. We keep the same cavity dimensions ($R = 6.25\lambda$ and $h = 16.67\lambda$) as before which, to accommodate a third QE, requires a reduction of the inter-emitter distances to $d_{12} = d_{23} = d = 1.17\lambda$ (where the extremal QEs are labeled as 1 and 3, and the central one as 2).

To proceed with the cavity design maximizing F_{+++}, the fidelity to the state in Eq. (6), we must first set the external parameters (driving amplitudes and emitter detunings) of the Liouvillian. In the case of QE pairs, these were set in accordance with recent literature [44]. We do not have such analytical insight in QE triples, and need to use a different approach. Operating at the master equation level, we perform a particle-swarm-optimization (PSO) [65] of its parameters, taking F_{+++} as the objective function. Imposing invariance under the exchange of QEs 1 and 3, ten quantities remain to be optimized: six internal ones, describing the emitter–emitter interactions and decay rates, and four external ones. To limit the range of parameter values, we used the EM dyadic Green's function for a bulk medium with $\epsilon_{\max} = 9$ (threshold permittivity in the TO algorithm) to estimate the spatial variation they can experience within the inter-emitter distance, d. In this way, we found that the conditions $\mathrm{sign}\{g_{12,23}\} = -\mathrm{sign}\{g_{13}\}$ and $\mathrm{sign}\{\gamma_{12,23}\} = -\mathrm{sign}\{\gamma_{13}\}$ had to be fulfilled. Our PSO computation in the constrained 10-dimensional parameter space involved 2×10^3 particles, up to 5×10^3 iteration steps, and 1000 runs under different initializations. The quantum steady state obtained this way presents a fidelity $F_{+++} = 0.91$ and a purity $P = 0.99$, indicating that it corresponds to a pure state of the QE triple slightly different from Eq. (6). This PSO procedure does not only allow us to benchmark the performance of our TO algorithm, it also provides us with the four external parameters that it requires: the QE-laser detunings, $\delta_{1,3}/\gamma_0 = 0.55$ and $\delta_2/\gamma_0 = -0.3$, and laser amplitudes, $\Omega_{1,3}/\gamma_0 = 0.33$ and $\Omega_2/\gamma_0 = -0.73$.

Figure 5(a) shows the map $\epsilon(\mathbf{r})$ maximizing F_{+++}. In contrast to the PSO described above, no QE symmetries are imposed in the TO algorithm and, hence, in the TO cavity itself. Its structure resembles very much that in Fig. 3(b), presenting periodic reflectors with high permittivity contrast and a larger, $\epsilon \sim 2$, background near its boundaries than at the central region, where $\epsilon \sim 1$. Remarkably, $\epsilon_{\max} = 3.6$, lower than that in Fig. 3(b). This originates from the shorter inter-emitter distance, as the cavities for Bell state preparation at $d_{12} \simeq d = 1.17\lambda$ (not shown) present a permittivity range very similar to that in Fig. 5(a). The main panel of Fig. 5(b) shows the tomography of the steady-state density matrix hosted by the dielectric cavity in panel (a). It is restricted to the ground

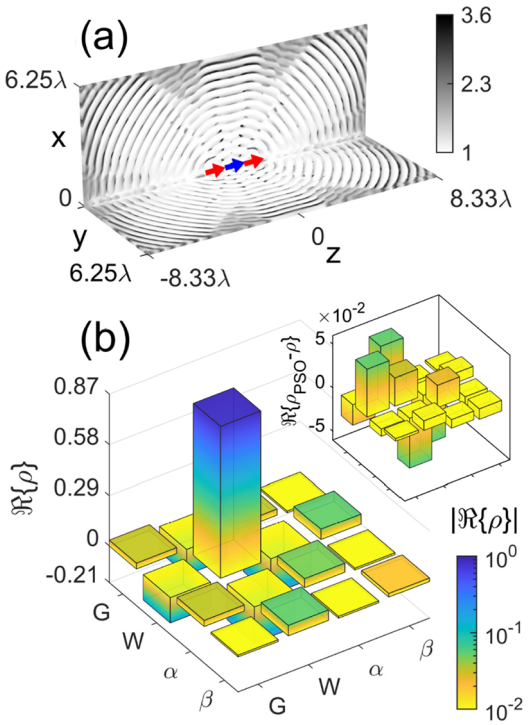

Fig. 5. (a) Permittivity map for the inverse-designed cavity maximizing the fidelity to the W state in Eq. (6) for an inter-emitter distance $d = 1.17\lambda$, and the same dimensions as the device in Fig. 3(b). The dielectric constant is coded in white-to-black linear scale. The position and orientation of the emitters along the z-direction is indicated by red and blue arrows. (b) Quantum tomography of the steady-state density matrix (real part) for a QE triple in the cavity in panel (a). Only the entries within the ground and single-excitation manifolds are shown. The colors represent the absolute value of the real part of the density matrix in logarithmic scale. Inset shows the difference between the TO density matrix and a phenomenological one, resulting from the direct PSO of the master equation parameters maximizing F_{+++} (same color scale as in the main panel).

and the single excitation manifolds, where the basis is formed by $|+++\rangle$ and the states $|\alpha\rangle = \frac{1}{\sqrt{3}}[|gge\rangle - a|geg\rangle - b|egg\rangle]$ and $|\beta\rangle = \frac{1}{\sqrt{3}}[|gge\rangle - b|geg\rangle - a|egg\rangle]$, with $a = (1+\sqrt{3})/2$ and $b = (1-\sqrt{3})/2$. The vertical axis displays the real part of population and coherence, and the color scale codes its absolute value in logarithmic scale. By simple inspection, we can extract $F_{+++} = \langle +++|\rho|+++\rangle = 0.87$, whose discrepancy ($\sim 0.04$) with that for the PSO Liouvillian is very similar to the deviation of $F_{+\pm}$ from unity in Fig. 2(a). Thus, we can conclude that the performance of the cavities is similar in both cases. To further verify the similarity between the quantum state in the TO device and its PSO counterpart, in the inset of Fig. 5(a), we present the tomography of the difference between the two density matrices. The deviations are most apparent in the W-state population and its coherence with the ground state, and these remain in the same range, below 0.05.

Finally, we analyze in more detail the nature of the QE-triple state implemented by the nanophotonic cavity. It presents a large purity, $P = 0.94$, and the single excitation section of the tomography in Fig. 5(b) indicates that the state amplitudes in the bare basis are not equal, in contrast to $|+++\rangle$. The calculation of the populations in this basis yield $\langle gge|\rho|gge\rangle = 0.210$, $\langle geg|\rho|geg\rangle = 0.527$, and $\langle egg|\rho|egg\rangle = 0.204$, revealing that the weight of QE 2 is larger than the two extremal ones. Notice the small discrepancy between the populations of the latter, a direct consequence of the slightly asymmetric character of $\epsilon(\mathbf{r})$. As discussed above, the degree of entanglement of W states exhibit a strong robustness against the disposal of one of the qubits. Indeed, the bipartite states that result from the tracing out of one of the QEs, $\rho^{(k)} = \mathrm{Tr}_k\{\rho\}$ (where $k = 1, 2, 3$), in Eq. (6), present a significant Wootters concurrence [66], $C(\rho^{(k)}) = 2/3 = 0.667$ for all k. Here, $C = 1$ for a maximally entangled two-qubit state, such as the Bell states in Eq. (3). The concurrence calculation for the partial traces of the density matrix in Fig. 5(b) yields $C(\rho^{(1)}) = 0.624$, $C(\rho^{(2)}) = 0.344$, $C(\rho^{(3)}) = 0.632$. Thus, the degree of bipartite entanglement obtained by tracing out the extremal QEs is similar to that in the perfectly symmetric W state. However, it is slightly lower if the intermediate QE is lost. This evidences the higher sensitivity to decoherence effects in the intermediate emitter of the quantum state in the inverse-designed TO cavity.

4. CONCLUSION

To conclude, we have generated pure quantum steady states of QE pairs and triples under coherent driving conditions through the inverse-design of their dielectric environment. By means of a topology-optimization algorithm that acts at the level of the electromagnetic dyadic Green's function, we have obtained nanophotonic cavities that engineer simultaneously the coherent and dissipative interactions between the emitters and their radiative decay. First, we have performed a thorough study of the capability of our devices to prepare even and odd Bell states, showing that they exploit a dissipation-driven mechanism to entangle pairs of quantum emitters separated several natural wavelengths apart. Analyzing the population dynamics in the system, we have shown that the small discrepancy between the pure states hosted by the cavities and exact Bell states translates into shorter preparation times. Finally, we have tested the versatility of our approach by applying it to a triple of quantum emitters, successfully realizing a highly entangled tripartite state akin to a symmetric W state. We believe that our results prove that inverse design is a powerful tool for the conception, implementation and refinement of quantum hardware based on nanophotonic platforms, with applications in areas such as for quantum sensing or metrology [67,68], and with potential advantages in terms of scalability and speed of operation with respect to other enabling technologies.

Funding. HORIZON EUROPE Framework Programme (101070700 (MIRAQLS)); Fundación BBVA; Comunidad de Madrid (Y2020/TCS-6545); Ministerio de Ciencia, Innovación y Universidades (CEX2023-001316-M, PID2021-126964OB-I00, PID2021-127968NB-I00, TED2021-130552B-C21, TED2021-130552B-C22).

Acknowledgments. We thank Alejandro Vivas-Viaña and Carlos Sánchez Muñoz for fruitful discussions.

Disclosures. The authors declare no conflicts of interest.

Data availability. Data and code underlying the results presented in this paper may be obtained from the authors upon reasonable request.

REFERENCES

1. V. Giannini, A. I. Fernández-Domínguez, S. C. Heck, *et al.*, "Plasmonic nanoantennas: fundamentals and their use in controlling the radiative properties of nanoemitters," Chem. Rev. **111**, 3888–3912 (2011).

2. D. E. Chang, J. S. Douglas, A. González-Tudela, *et al.*, "Colloquium: quantum matter built from nanoscopic lattices of atoms and photons," Rev. Mod. Phys. **90**, 031002 (2018).
3. A. W. Elshaari, W. Pernice, K. Srinivasan, *et al.*, "Hybrid integrated quantum photonic circuits," Nat. Photonics **14**, 285–298 (2020).
4. A. González-Tudela, A. Reiserer, J. J. García-Ripoll, *et al.*, "Light–matter interactions in quantum nanophotonic devices," Nat. Rev. Phys. **6**, 166 (2024).
5. R. Mitsch, C. Sayrin, B. Albrecht, *et al.*, "Quantum state-controlled directional spontaneous emission of photons into a nanophotonic waveguide," Nat. Commun. **5**, 5713 (2014).
6. M. K. Bhaskar, D. D. Sukachev, A. Sipahigil, *et al.*, "Quantum nonlinear optics with a germanium-vacancy color center in a nanoscale diamond waveguide," Phys. Rev. Lett. **118**, 223603 (2017).
7. C. Groiseau, A. I. Fernández-Domínguez, D. Martín-Cano, *et al.*, "Single-photon source over the terahertz regime," PRX Quantum **5**, 010312 (2024).
8. F. Najafi, J. Mower, N. C. Harris, *et al.*, "On-chip detection of non-classical light by scalable integration of single-photon detectors," Nat. Commun. **6**, 5873 (2015).
9. A. Sipahigil, R. E. Evans, D. D. Sukachev, *et al.*, "An integrated diamond nanophotonics platform for quantum-optical networks," Science **354**, 847–850 (2016).
10. J. Q. Grim, A. S. Bracker, M. Zalalutdinov, *et al.*, "Scalable in operando strain tuning in nanophotonic waveguides enabling three-quantum-dot superradiance," Nat. Mater. **18**, 963–969 (2019).
11. P. Lodahl, S. Mahmoodian, S. Stobbe, *et al.*, "Chiral quantum optics," Nature **541**, 473–480 (2017).
12. A. Blanco-Redondo, "Topological nanophotonics: toward robust quantum circuits," Proc. IEEE **108**, 837–849 (2020).
13. S. L. Mouradian, T. Schröder, C. B. Poitras, *et al.*, "Scalable integration of long-lived quantum memories into a photonic circuit," Phys. Rev. X **5**, 031009 (2015).
14. L. Ostermann, D. Plankensteiner, H. Ritsch, *et al.*, "Protected subspace Ramsey spectroscopy," Phys. Rev. A **90**, 053823 (2014).
15. A. González-Tudela, C.-L. Hung, D. E. Chang, *et al.*, "Subwavelength vacuum lattices and atom–atom interactions in two-dimensional photonic crystals," Nat. Photonics **9**, 320–325 (2015).
16. C. Tabares, A. Muñoz de las Heras, L. Tagliacozzo, *et al.*, "Variational quantum simulators based on waveguide QED," Phys. Rev. Lett. **131**, 073602 (2023).
17. S. Molesky, Z. Lin, A. Y. Piggott, *et al.*, "Inverse design in nanophotonics," Nat. Photonics **12**, 659–670 (2018).
18. S. So, T. Badloe, J. Noh, *et al.*, "Deep learning enabled inverse design in nanophotonics," Nanophotonics **9**, 1041–1057 (2020).
19. A. Y. Piggott, J. Lu, K. G. Lagoudakis, *et al.*, "Inverse design and demonstration of a compact and broadband on-chip wavelength demultiplexer," Nat. Photonics **9**, 374–377 (2015).
20. Z. Lin, X. Liang, M. Lončar, *et al.*, "Cavity-enhanced second-harmonic generation via nonlinear-overlap optimization," Optica **3**, 233–238 (2016).
21. Z. Lin, A. Pick, M. Lončar, *et al.*, "Enhanced spontaneous emission at third-order Dirac exceptional points in inverse-designed photonic crystals," Phys. Rev. Lett. **117**, 107402 (2016).
22. Z. Kuang and O. D. Miller, "Computational bounds to light–matter interactions via local conservation laws," Phys. Rev. Lett. **125**, 263607 (2020).
23. P. Chao, B. Strekha, R. Kuate Defo, *et al.*, "Physical limits in electromagnetism," Nat. Rev. Phys. **4**, 543–559 (2022).
24. P. R. Wiecha, A. Arbouet, C. Girard, *et al.*, "Deep learning in nano-photonics: inverse design and beyond," Photonics Res. **9**, B182–B200 (2021).
25. G.-X. Liu, J.-F. Liu, W.-J. Zhou, *et al.*, "Inverse design in quantum nanophotonics: combining local-density-of-states and deep learning," Nanophotonics **12**, 1943–1955 (2023).
26. A. Miguel-Torcal, J. Abad-Arredondo, F. J. García-Vidal, *et al.*, "Inverse-designed dielectric cloaks for entanglement generation," Nanophotonics **11**, 4387–4395 (2022).
27. E. G. Melo, W. Eshbaugh, E. B. Flagg, *et al.*, "Multiobjective inverse design of solid-state quantum emitter single-photon sources," ACS Photonics **10**, 959–967 (2023).
28. J. Yang, M. A. Guidry, D. M. Lukin, *et al.*, "Inverse-designed silicon carbide quantum and nonlinear photonics," Light: Sci. Appl. **12**, 201 (2023).
29. M. P. Bendsoe and O. Sigmund, *Topology Optimization: Theory, Methods, and Applications* (Springer Science & Business Media, 2003).
30. J. Jensen and O. Sigmund, "Topology optimization for nano-photonics," Laser Photonics Rev. **5**, 308–321 (2011).
31. D. Sych and G. Leuchs, "A complete basis of generalized Bell states," New J. Phys. **11**, 013006 (2009).
32. A. Vivas-Viaña, A. González-Tudela, and C. S. Muñoz, "Unconventional mechanism of virtual-state population through dissipation," Phys. Rev. A **106**, 012217 (2022).
33. W. Dür, G. Vidal, and J. I. Cirac, "Three qubits can be entangled in two inequivalent ways," Phys. Rev. A **62**, 062314 (2000).
34. H. T. Dung, L. Knöll, and D.-G. Welsch, "Resonant dipole-dipole interaction in the presence of dispersing and absorbing surroundings," Phys. Rev. A **66**, 063810 (2002).
35. H.-P. Breuer and F. Petruccione, *The Theory of Open Quantum Systems* (Oxford University Press, 2007).
36. L. Novotny and B. Hecht, *Principles of Nano-Optics*, 2nd ed. (Cambridge University Press, 2012).
37. D. Dzsotjan, A. S. Sorensen, and M. Fleischhauer, "Quantum emitters coupled to surface plasmons of a nanowire: a Green's function approach," Phys. Rev. B **82**, 075427 (2010).
38. A. Gonzalez-Tudela, D. Martin-Cano, E. Moreno, *et al.*, "Entanglement of two qubits mediated by one-dimensional plasmonic waveguides," Phys. Rev. Lett. **106**, 020501 (2011).
39. R. Jozsa, "Fidelity for mixed quantum states," J. Mod. Opt. **41**, 2315–2323 (1994).
40. S. Mignuzzi, S. Vezzoli, S. A. R. Horsley, *et al.*, "Nanoscale design of the local density of optical states," Nano Lett. **19**, 1613–1617 (2019).
41. R. Bennett and S. Y. Buhmann, "Inverse design of light–matter interactions in macroscopic QED," New J. Phys. **22**, 093014 (2020).
42. R. Bennett, "Inverse design of environment-induced coherence," Phys. Rev. A **103**, 013706 (2021).
43. J. Cambiasso, G. Grinblat, Y. Li, *et al.*, "Bridging the gap between dielectric nanophotonics and the visible regime with effectively lossless gallium phosphide antennas," Nano Lett. **17**, 1219–1225 (2017).
44. H. Pichler, T. Ramos, A. J. Daley, *et al.*, "Quantum optics of chiral spin networks," Phys. Rev. A **91**, 042116 (2015).
45. M. A. Nielsen and I. L. Chuang, *Quantum Computation and Quantum Information: 10th Anniversary Edition* (Cambridge University Press, 2010).
46. Z. Ficek and R. Tanaś, "Entangled states and collective nonclassical effects in two-atom systems," Phys. Rep. **372**, 369–443 (2002).
47. A. Canaguier-Durand, R. Pierrat, and R. Carminati, "Cross density of states and mode connectivity: probing wave localization in complex media," Phys. Rev. A **99**, 013835 (2019).
48. A. F. Alharbi and Z. Ficek, "Deterministic creation of stationary entangled states by dissipation," Phys. Rev. A **82**, 054103 (2010).
49. M. J. Kastoryano, F. Reiter, and A. S. Sørensen, "Dissipative preparation of entanglement in optical cavities," Phys. Rev. Lett. **106**, 090502 (2011).
50. H. Zheng and H. U. Baranger, "Persistent quantum beats and long-distance entanglement from waveguide-mediated interactions," Phys. Rev. Lett. **110**, 113601 (2013).
51. A. Vivas-Viaña, D. Martín-Cano, and C. S. Muñoz, "Dissipative stabilization of maximal entanglement between non-identical emitters via two-photon excitation," arXiv, (2023).
52. T. Ramos, H. Pichler, A. J. Daley, *et al.*, "Quantum spin dimers from chiral dissipation in cold-atom chains," Phys. Rev. Lett. **113**, 237203 (2014).
53. T. Ramos, B. Vermersch, P. Hauke, *et al.*, "Non-Markovian dynamics in chiral quantum networks with spins and photons," Phys. Rev. A **93**, 062104 (2016).
54. M. B. Plenio, S. F. Huelga, A. Beige, *et al.*, "Cavity-loss-induced generation of entangled atoms," Phys. Rev. A **59**, 2468–2475 (1999).

55. D. Manzano and P. Hurtado, "Harnessing symmetry to control quantum transport," Adv Phys **67**, 1–67 (2018).
56. V. V. Albert and L. Jiang, "Symmetries and conserved quantities in Lindblad master equations," Phys. Rev. A **89**, 022118 (2014).
57. I. Medina, F. J. García-Vidal, A. I. Fernández-Domínguez, *et al.*, "Few-mode field quantization of arbitrary electromagnetic spectral densities," Phys. Rev. Lett. **126**, 093601 (2021).
58. M. Sánchez-Barquilla, F. J. García-Vidal, A. I. Fernández-Domínguez, *et al.*, "Few-mode field quantization for multiple emitters," Nanophotonics **11**, 4363–4374 (2022).
59. R.-Q. Li, D. Hernángomez-Pérez, F. García-Vidal, *et al.*, "Transformation optics approach to plasmon-exciton strong coupling in nanocavities," Phys. Rev. Lett. **117**, 107401 (2016).
60. G. McCauley, B. Cruikshank, D. I. Bondar, *et al.*, "Accurate Lindblad-form master equation for weakly damped quantum systems across all regimes," npj Quantum Inf. **6**, 74 (2020).
61. A. R. R. Carvalho, F. Mintert, and A. Buchleitner, "Decoherence and multipartite entanglement," Phys. Rev. Lett. **93**, 230501 (2004).
62. N. Brunner, J. Sharam, and T. Vértesi, "Testing the structure of multipartite entanglement with Bell inequalities," Phys. Rev. Lett. **108**, 110501 (2012).
63. A. Acín, D. Bruß, M. Lewenstein, *et al.*, "Classification of mixed three-qubit states," Phys. Rev. Lett. **87**, 040401 (2001).
64. L. Borsten, D. Dahanayake, M. J. Duff, *et al.*, "Freudenthal triple classification of three-qubit entanglement," Phys. Rev. A **80**, 032326 (2009).
65. M. R. Bonyadi and Z. Michalewicz, "Particle swarm optimization for single objective continuous space problems: a review," Evol. Comput. **25**, 1–54 (2017).
66. W. K. Wootters, "Entanglement of formation of an arbitrary state of two qubits," Phys. Rev. Lett. **80**, 2245–2248 (1998).
67. J. Franke, S. R. Muleady, R. Kaubruegger, *et al.*, "Quantum-enhanced sensing on optical transitions through finite-range interactions," Nature **621**, 740–745 (2023).
68. W. J. Eckner, N. Darkwah Oppong, A. Cao, *et al.*, "Realizing spin squeezing with Rydberg interactions in an optical clock," Nature **621**, 734–739 (2023).